



**HAL**  
open science

# Effect of cutting tool geometry on hole quality in orbital drilling

Pierre-André Rey, Johanna Senatore, Yann Landon

► **To cite this version:**

Pierre-André Rey, Johanna Senatore, Yann Landon. Effect of cutting tool geometry on hole quality in orbital drilling. *International Journal of Advanced Manufacturing Technology*, 2023, 10.1007/s00170-023-12539-y . hal-04292258

**HAL Id: hal-04292258**

**<https://hal.science/hal-04292258>**

Submitted on 17 Nov 2023

**HAL** is a multi-disciplinary open access archive for the deposit and dissemination of scientific research documents, whether they are published or not. The documents may come from teaching and research institutions in France or abroad, or from public or private research centers.

L'archive ouverte pluridisciplinaire **HAL**, est destinée au dépôt et à la diffusion de documents scientifiques de niveau recherche, publiés ou non, émanant des établissements d'enseignement et de recherche français ou étrangers, des laboratoires publics ou privés.



# Effect of cutting tool geometry on hole quality in orbital drilling

Pierre-André Rey<sup>1</sup> · Johanna Senatore<sup>2</sup> · Yann Landon<sup>2</sup>

Received: 16 September 2022 / Accepted: 18 October 2023

© The Author(s), under exclusive licence to Springer-Verlag London Ltd., part of Springer Nature 2023

## Abstract

The orbital drilling process is a very complex machining operation. Due to the helical path of the tool in the material and the tool geometry that can be very complex, the geometry of the chip is very variable along the cutting edge and during a revolution of the tool. This complexity leads to variable cutting forces during drilling and makes it difficult to model and estimate for different tool geometries.

The aim of this study is, therefore, to use a modelling of the orbital drilling process in order to study the influence of the geometry of the tool and the cutting conditions on the cutting forces. The final objective is to identify their impact on the quality of the drilled hole and, thus, to control the final quality.

First, the chip geometry is modelled from the cutting parameters and the macro-geometry of the tool. It needs to determine the tooth trajectory into the material for each point of the cutting edge. Cutting force models, based on the instantaneous chip thickness, are then implemented. An experimental study validates the modelling by cutting force measurements carried out during orbital drilling tests. From this modelling, it is now possible to study the influence of the geometry of the cutting tool on the forces in order to control the loading on the tool and therefore the final quality of the drilled hole.

**Keywords** Orbital drilling · 3D chip geometry simulation · Tool geometry optimization

## 1 Introduction

For mechanical assembly of structures, the drilling of the fastening holes is an important matter. Especially in the aeronautical industry, the drilling process must reach not only high-level requirements about hole quality and material integrity control but also economical target in terms of productivity [1, 2]. It explains the constant interest brought to the drilling process by academic researchers as through industrial solution developments. According to the increasing diversity of materials used in aircraft structures and their different characteristics, the process had to evolve to allow the drilling of holes in multi-material stacks made of highly different materials as composite laminates, titanium alloys, aluminum alloys etc. [3, 4]. A number of research studies

have been brought on the characterization of new solutions in terms of cutting tools technologies and of processes as vibration-assisted drilling [5, 6] or, more recently, the development of smart drilling [7]. Among these solutions, the orbital drilling process can be cited. Orbital drilling, also called helical milling, involves making a hole with a tool of a diameter smaller than the diameter of the hole, driven on a helical path (Fig. 1).

Developed at the beginning for wood drilling, it has been brought to industrial application for metal drilling and then composite drilling for different reasons. First, it allows the drilling of different diameter holes with the same tool [4]. Also, the interrupted cutting process occurring in orbital drilling leads to a good chip fragmentation, and thus to an easier and improved chip evacuation through the radial gap between the tool and the borehole surface [8]. It can be added that this process generates low cutting forces that lead to a reduction of classical drilling defects as burrs in metallic materials or delamination in composite laminates [4, 9, 10]. Moreover, this process is also justified for drilling titanium alloys [11]. But its use has been also reduced because of the drilling duration and the more complex control of the trajectory (with tool deflection issue) [8]. Nevertheless, from a global economic point

✉ Pierre-André Rey  
pierre-andre.rey@ensam.eu

<sup>1</sup> Institut de mécanique et d'ingénierie, CNRS UMR 5295, Arts et Métiers ParisTech - Campus de Bordeaux, Esp. des Arts et Métiers, 33405 Talence, France

<sup>2</sup> Institut Clément Ader, CNRS UMR 5312, Université Paul Sabatier, 3 rue Caroline Aigle, 31400 Toulouse, France

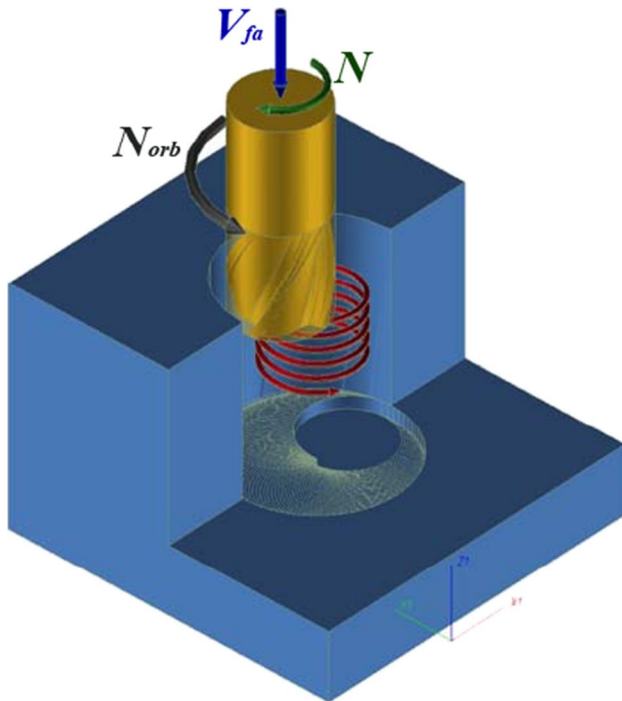


Fig. 1 Orbital drilling

of view, the orbital drilling process may permit to reduce the number of operations to reach the finished hole. In that case, it appears to be more productive to obtain the final hole in one operation of orbital drilling rather than in 2 or 3 operations of axial drilling and reaming. And considering the matter of trajectory programming, industrial solutions have been developed for this purpose, proposing orbital drilling units with an eccentric spindle [12]. The impact on the microstructure and the fatigue behavior of drilled aerostructures was also studied, and Sun et al. [13] showed that orbital drilling has to be well optimized to reach the same level of fatigue behavior the one obtains with axial drilling. After that, the control of the hole quality has to be done through an optimization of the process: cutting conditions and tool geometry [14]. Ozturk et al. [15] proposed a unified mathematical model which predicts

three-dimensional chatter stability as a function of orbital pitch length, spindle speed, and orbital speed of the tool and permits the optimization of the cutting conditions. Considering tool geometry, the influence of both axial and tangential feeds on the hole diameter has been investigated for simple flat-end tools [4, 16] based on a simple modelling of the chip geometry in orbital drilling dedicated to these simple-shape tools. For more complex tool geometries, another model of chip geometry and cutting forces was developed and proposed by Rey et al. [17] or, more recently, by Zhou et al. [18]. The tool geometry was introduced into the modelling by considering local cutting conditions (cutting speed gradient along the cutting edges) and forces. The tool geometry was firstly expressed analytically before being divided into elementary edge portions. On each portion, a local cutting force model was applied. The elementary forces were then summed according to the evolution of the edge geometry. Finally, this model makes it possible to simulate the geometry of the instantaneous chip. The cutting forces simulation is then possible as a function of the geometry of the tool considered and permits to highlight the important role of the shape of the axial part of the tool. This allows a better understanding of cutting phenomena occurring in orbital drilling (e.g., tool deflection). This model can be used to optimize the cutting conditions and the tool geometry in relation to the cutting forces generated. Based on this type of modelling, Zhou et al. [19] proposed an analysis of the chip-splitting performance of a dedicated cutting tool in dry orbital drilling. In this paper, this model is used to simulate the impact of different tool geometries in order to give a better understanding of the role of each part of the tool. A tool optimization is then possible. The results are discussed and compared to experimental tests for validation.

## 2 Kinematic modelling of orbital drilling

The modelling of the cutting forces by a semi-analytical approach used in this paper is based on the work of Rey et al. [17] and is summarized in this paper. It requires precise

Fig. 2 Representation of the cutting-edge profile

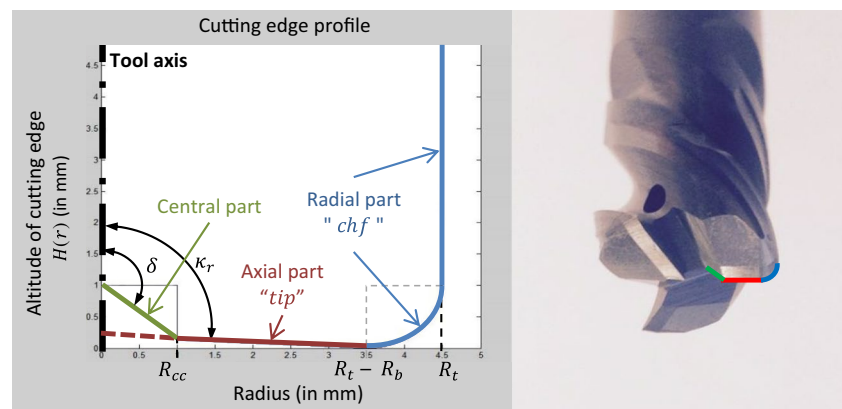


**Table 1** Geometrical parameters of the tool

Tool radius	$R_t$
Number of teeth	$Z$
Number of teeth with center-cut	$Z_{cc}$
Corner radius	$R_b$
Radius without center-cut	$R_{cc}$
Tool cutting edge angle	$\kappa_r$

knowledge of the chip geometry. To carry out a model of the chip geometry, it is necessary to define the input data of this model as well as the references which will be used. The geometry of the tool, with the definition of the profile of the cutting edge, and the cutting parameters are first defined. The calculation of the instantaneous chip section is then developed. In the present study, the drilling operation was simulated by down-milling but the model developed could also be used for up-milling.

### 2.1 Geometrical definition of orbital drilling

#### 2.1.1 Definition and modelling of the tool geometry

The tool considered in this study is the one of Rey et al. [17]. Its macro-geometry (Fig. 2) is defined using the following parameters (Table 1):

Each cutting edge is discretized into two parts: the radial part noted “*chf*,” and the axial part noted “*tip*,” which includes the central part when the tool is without center-cut.

A function  $H(r)$  is established in order to define analytically the edge profile. It allows to give the altitude along the tool axis of each point of the edge versus the radius  $r$ . The lowest tool point is defined at the altitude  $Z=0$ . The function  $H(r)$  is decomposed into several functions to take into consideration the different parts of the edge:

- Central part if  $0 < r < R_{cc}$  :

$$H(r) = (R_{cc} - (R_t - R_b)) \times \tan\left(\frac{\pi}{2} - \kappa_r\right) + (R_{cc} - r) \times \tan\left(\delta - \frac{\pi}{2}\right)$$

with  $\delta = \kappa_r$  in the case of the edge with center-cut (red dotted line on Fig. 2)

- Axial part (*tip*): if  $R_{cc} < r < R_t - R_b$  :

$$H(r) = [r - (R_t - R_b)] \cdot \tan\left(\frac{\pi}{2} - \kappa_r\right)$$

- Radial part (*chf*) if  $R_t - R_b < r < R_t$  :

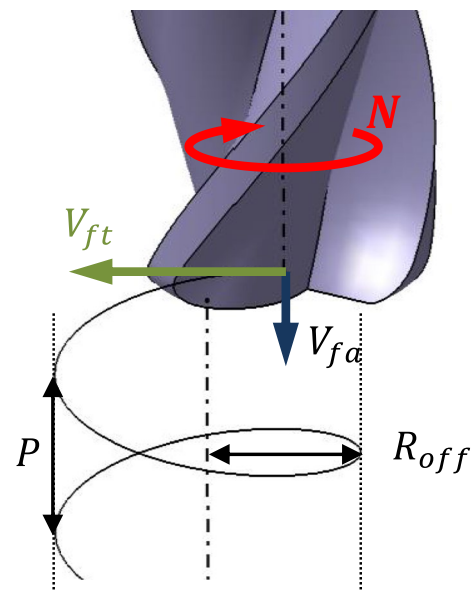


**Fig. 3** Feed definition

$$H(r) = R_b - \sqrt{R_b^2 - [r - (R_t - R_b)]^2}$$

The surface ( $A_i$ ) of revolution of the tool can now be modelled [17] (Fig. 5).

#### 2.1.2 Definition of cutting parameters

The helical trajectory of the tool in orbital drilling can be decomposed into an axial feed  $f_a$  and a tangential feed  $f_t$  (Fig. 3). The cutting parameters are thus presented in Table 2.

**Table 2** Process parameters for orbital drilling

Drilling radius	$R_h$
Interpolation radius, called offset	$R_{off} = R_h - R_t$
Pitch	$P$
Cutting speed	$V_c$
Tool revolution speed (rev/min)	$N = \frac{V_c}{2\pi \times R_t}$
Axial feed (mm/rev)	$f_a$
Axial feed per tooth (mm/tooth)	$f_{za} = \frac{f_a}{Z}$
Axial feed speed (mm/min)	$V_{fa} = f_{za} \times N$
Tangential feed (mm/rev)	$f_t$
Tangential feed per tooth (mm/rev/tooth)	$f_{zt} = \frac{f_t}{Z}$
Tangential feed speed (mm/min)	$V_{ft} = f_{zt} \times N$
Orbital revolution speed	$N_{orb} = \frac{V_h}{2\pi \times R_{off}}$

## 2.2 Calculation of the instantaneous chip section

### 2.2.1 References definition

- Machine reference: fixed

$$R_m = (HL_i, X, Y, Z)$$

- Orbital reference: permits to define the tool position “*i*” on the helical trajectory. This reference is described by the tool angular position  $\theta_i$  in relation to the machine reference

$$R_{oi} = (HL_i, X_{oi}, Y_{oi}, Z)$$

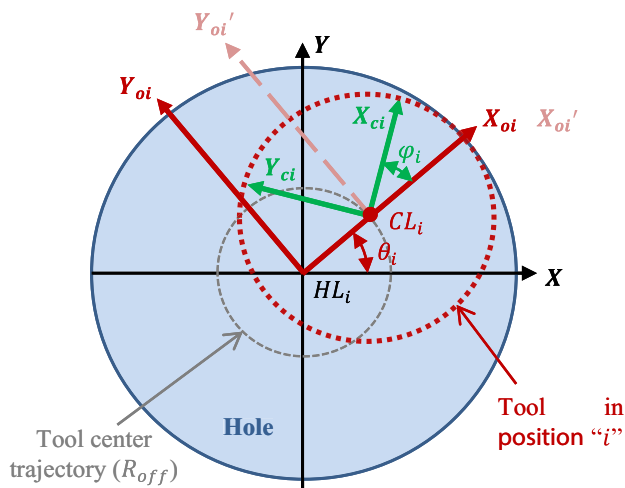
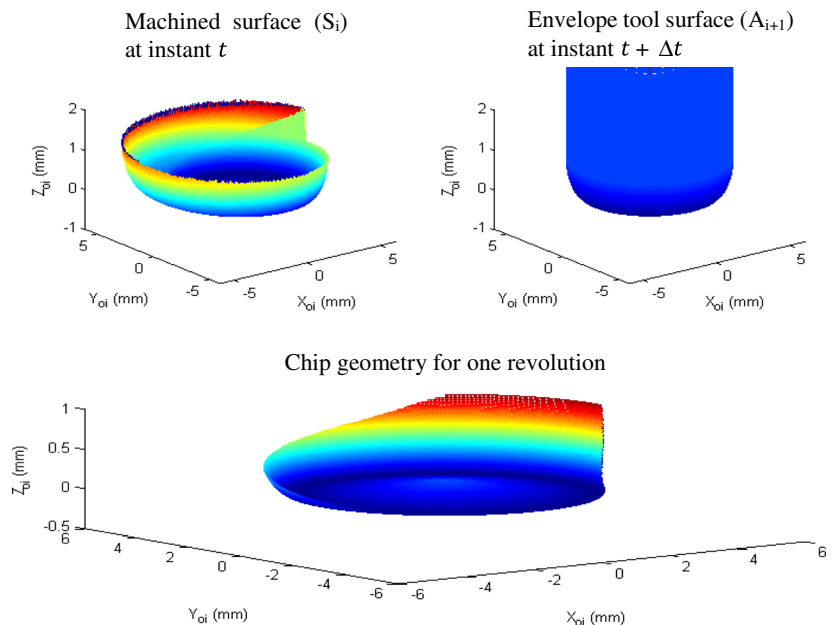


Fig. 4 References definition

Fig. 5 3D visualisation of the chip ( $V_c = 30 \text{ m/min}$ ;  $f_{za} = 0.005 \text{ mm/tooth}$ ;  $f_{zd} = 0.04 \text{ mm/tooth}$ )



- Tool reference: described by the angular position  $\varphi_i$  of the considered point of the tool in the tool revolution

$$R_t = (CL_i, X_{ci}, Y_{ci}, Z)$$

### 2.2.2 Modelling of chip volume and calculation of the instantaneous chip section

In order to determine the chip section, the machined surface at instant (*t*) is firstly defined. This machined surface (*S<sub>i</sub>*) is modelled by scanning the envelope surface of revolution of the tool (*A*) on the helical trajectory (Fig. 4).

The position of the tool in the next moment (*t* +  $\Delta t$ ) is defined by a step along the trajectory calculated from the tooth feed. The surface obtained is the surface of revolution (*A<sub>i+1</sub>*) of the tool on this new position.

The chip geometry between (*t*) and (*t* +  $\Delta t$ ) is calculated by making the difference between these two surfaces (Fig. 5).

The instantaneous chip section is given by cross-section of the chip modelled (Fig. 6).

The chip section obtained is discretized along the cutting edge into elementary chips of thickness *h<sub>i</sub>* (normal to the edge profile) and of width *b<sub>i</sub>*.

The calculation of the volume of material removed and the geometry of the instantaneous chip are more detailed in Rey et al. [17].

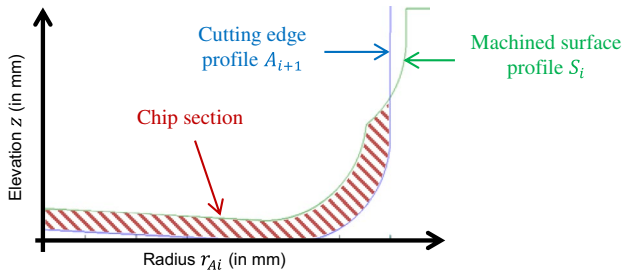


Fig. 6 Instantaneous chip section

### 3 Cutting forces modelling

In this work, a semi-analytical cutting model is chosen as it permits to reduce the number of coefficients and calibration tests [20, 21]. The model of Rey et al. [17] is used in this work. Knowing the instantaneous chip section, the cutting forces applied on the tool during drilling can be expressed. For this, the local forces “ $dF$ ” on each discrete chip element are modelled as follows:

$$dF = K^* \times h \times b \tag{1}$$

where  $K^*$  is a specific cutting coefficient. As the chip thickness ( $h_i$ ) is highly variable along the cutting edge and during the tool revolution, the specific cutting coefficient is considered non-constant [22, 23] and estimated by the following function [24]:

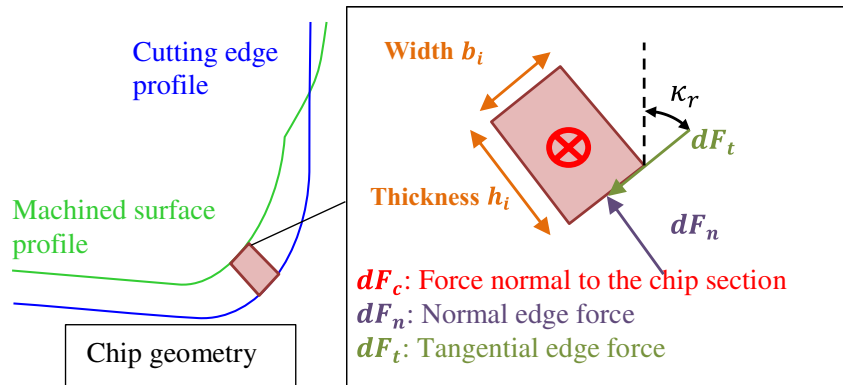
$$K^* = K \times h^{-q} \tag{2}$$

with  $K$  and  $q$  as two constants

Thus three elementary forces applied on the tool are defined (Fig. 7):

$$\begin{cases} dF_c = K_c \times h_i^{1-q_c} \times b_i \\ dF_n = K_n \times h_i^{1-q_n} \times b_i \\ dF_t = K_t \times h_i^{1-q_t} \times b_i \end{cases} \tag{3}$$

Fig. 7 Local forces applied on the tool for a given chip section



where  $h_i$  and  $b_i$  are dependent on the angular position  $\varphi_i$  and on the radius  $r_{Ai}$ .

Considering that the chip geometry and the cutting speed are highly different in the axial part (noted “*tip*”) and the radial part (noted “*chf*”) of the tool (Fig. 2), the coefficients of the cutting force model are considered different (and identified separately with specific calibration tests). The modelling of the cutting forces becomes the following:

- if  $0 \leq r \leq R_t - R_b$ :
 
$$\begin{cases} dF_c = dF_{c\_tip}(r_{Ai}, \varphi_i) = K_{c\_tip} \times h_i(r_{Ai}, \varphi_i)^{1-q_{c\_tip}} \times b_i(r_{Ai}, \varphi_i) \\ dF_n = dF_{n\_tip}(r_{Ai}, \varphi_i) = K_{n\_tip} \times h_i(r_{Ai}, \varphi_i)^{1-q_{n\_tip}} \times b_i(r_{Ai}, \varphi_i) \\ dF_t = dF_{t\_tip}(r_{Ai}, \varphi_i) = K_{t\_tip} \times h_i(r_{Ai}, \varphi_i)^{1-q_{t\_tip}} \times b_i(r_{Ai}, \varphi_i) \end{cases} \tag{4}$$

- if  $R_t - R_b < r \leq R_t$ :
 
$$\begin{cases} dF_c = dF_{c\_chf}(r_{Ai}, \varphi_i) = K_{c\_chf} \times h_i(r_{Ai}, \varphi_i)^{1-q_{c\_chf}} \times b_i(r_{Ai}, \varphi_i) \\ dF_n = dF_{n\_chf}(r_{Ai}, \varphi_i) = K_{n\_chf} \times h_i(r_{Ai}, \varphi_i)^{1-q_{n\_chf}} \times b_i(r_{Ai}, \varphi_i) \\ dF_t = dF_{t\_chf}(r_{Ai}, \varphi_i) = K_{t\_chf} \times h_i(r_{Ai}, \varphi_i)^{1-q_{t\_chf}} \times b_i(r_{Ai}, \varphi_i) \end{cases} \tag{5}$$

#### 3.1 Modelling the cutting forces applied on the axial part of the tool

On the axial part, the cutting forces  $F_{c\_tip z}(\varphi_i)$ ,  $F_{n\_tip z}(\varphi_i)$ , and  $F_{t\_tip z}(\varphi_i)$  are calculated for each tooth  $z$  of the tool, taking into account the differences in the tooth profile which can exist (e.g., with or without center-cut) (Fig. 8 - Rey et al. [17]).

For this, 6 axial cutting parameters have to be identified:  $K_{c\_tip}$ ,  $K_{n\_tip}$ ,  $K_{t\_tip}$  and  $q_{c\_tip}$ ,  $q_{n\_tip}$ ,  $q_{t\_tip}$ . These parameters are considered to be the same for each tooth.

These force components only consider cutting mechanisms. But specific mechanisms may occur under the center of the tool as degraded cutting mechanisms or extrusion. To consider this phenomenon into the modelling, an axial indentation force is added to the model. The selected modelling is the one proposed by Williams for axial drilling [25]:

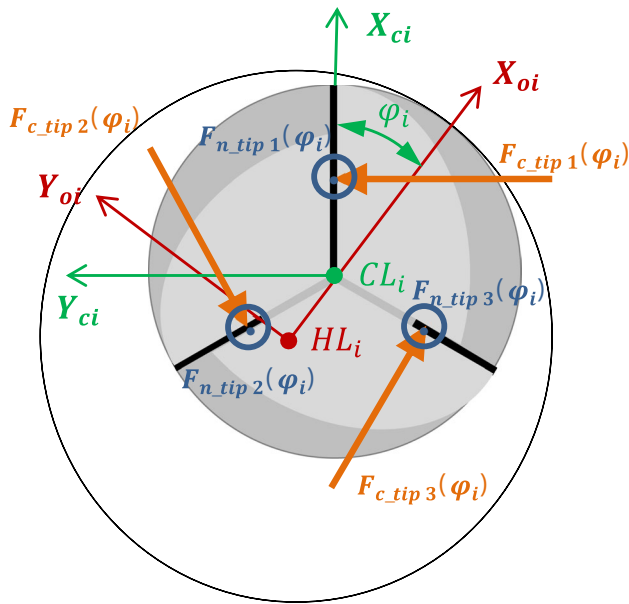


**Fig. 8** Representation of forces generated by the axial part of a tool with three teeth

$$F_{ind} = K_{ind} \times V_{fa}^{q_{ind}} \times S \tag{6}$$

where  $S$  is the projected surface of the indentation zone under the center of the tool. For a given tool,  $S$  can be considered a constant since the axial feed speed remains low [6, 25]. This is especially the case in orbital drilling. Thus, this parameter can be included into the coefficient  $K_{ind}$ .

### 3.2 Modelling the cutting forces applied on the radial part of the tool

On the radial part of the tool, the cutting forces  $F_{c\_chfz}(\varphi_i)$ ,  $F_{n\_chfz}(\varphi_i)$ , and  $F_{t\_chfz}(\varphi_i)$  are calculated for each tooth  $z$  of the tool (Fig. 8).

As for the axial part, 6 radial cutting parameters have to be identified.

The proposed modelling expresses the local cutting forces for each tooth of the tool. The axial part and the radial part of the tool have been dissociated in order to consider different cutting phenomena that occur under the tool tip and on the chamfer. The parameters of the modelling have to be identified separately for both parts in order to be able to simulate the global forces generated in orbital drilling.

### 3.3 Experimental setup

In this paper, the case of a three-flute tool ( $Z = 3$ ) of diameter  $D_t = 9$  mm, with a corner radius  $R_b = 1$  mm, and with a single tooth with center-cut ( $R_{cc} = 2.2$  mm) is presented.

The machined material was titanium alloy TiAl6V4 of 19-mm thick. The identification of the model parameters “ $K$ ” and “ $q$ ” was performed through calibration tests on a DMG DMU50eVo CNC machining center, equipped with a 24,000 rpm/25 kW spindle. The methodology for the identification of these coefficients is presented in Rey et al. [17]. The identified coefficients are summarized in Table 3.

It is difficult to compare these coefficients directly as different cutting mechanisms are involved and different chip thicknesses are encountered. In order to compare the results of the calibration phase, the equivalent coefficients  $K_c^*$  and  $K_n^*$  are calculated for a given value of  $h$  from (Eq. 2). It appears that the coefficients for the radial part of the tool are nearly twice as important as for the axial part. This can be explained by the differences in terms of cutting geometry. On the radial part and on the axial part of the tool, the rake and clearance angles are different. Moreover, the edge sharpness may also be different. But also, the cutting speed may explain a part of this difference. It can also be noted that coefficients  $K_c^*$  and  $K_n^*$  are nearly equal for a given part of the tool. This shows the importance of normal forces in orbital drilling, while cutting forces (normal to the chip section) are often considered preponderant. The influence of edge sharpness radius must also be considered and studied. Many studies have shown that this parameter could have a strong influence on cutting forces and more particularly on titanium alloys which are considered to have low machinability [26, 27]. It is recommended to have a low edge radius for this material to minimize the cutting forces. In this study, the edge radius was estimated for the axial part between  $r_\epsilon = 10$  to  $14 \mu\text{m}$  and for the radial part between  $r_\epsilon = 18$  to  $25 \mu\text{m}$ . These values could therefore partly explain the greater values of the coefficients of the radial part.

The validation of the model was done by comparing simulated forces and measured forces in orbital drilling of holes of diameter  $D_h = 11.1$  mm. For all tests (calibration and validation), cutting forces were recorded using the 6-component Kistler 9257B dynamometer and sampled at 10 kHz. The cutting conditions were variable for the experimental plan. Only the cutting speed  $V_c$  was kept at a constant value of 30 m/min (prescribed by the tool manufacturer to ensure the maximum tool life) as its influence on the cutting forces is negligible for small variations [4].

### 3.4 Result of the cutting forces modelling

First, from the identified coefficients, it is possible to simulate the forces applied on the axial part of the tool, considering the same parameters for the three teeth. For this,

the forces  $F_{c\_tip}$  and  $F_{n\_tip}$  are firstly projected along the axes  $Y_{oi}$  and  $X_{oi}$ . The resulting forces are respectively  $F_{T\_tip}$  (tangent to the borehole, along  $Y_{oi}$ ) and  $F_{R\_tip}$  (radial to the borehole, along  $X_{oi}$ ). The axial force  $F_{A\_tip}$  is obtained by adding the projection of  $F_{n\_tip}$  along axis  $Z$  and the indentation force  $F_{ind}$  (Fig. 9):

$$\begin{cases} F_{T\_tip} = \sum_{z=1}^Z [F_{c\_tip\ z} \times Y_{oi} + F_{n\_tip\ z} \times Y_{oi}] \\ F_{R\_tip} = -\sum_{z=1}^Z [F_{c\_tip\ z} \times X_{oi} + F_{n\_tip\ z} \times X_{oi}] \\ F_{A\_tip} = \sum_{z=1}^Z [F_{n\_tip\ z} \times Z] + F_{ind} \end{cases} \quad (7)$$

In the same manner, the forces  $F_{c\_chf}$  and  $F_{n\_chf}$ , applied on the radial part of the tool, are simulated and projected along the axis  $Y_{oi}$ ,  $X_{oi}$ , and  $Z$ . The resulting forces are respectively  $F_{T\_chf}$  (tangent to the borehole, along  $Y_{oi}$ ),  $F_{R\_chf}$  (radial to the borehole, along  $X_{oi}$ ), and  $F_{A\_chf}$  (axial force, along  $Z$ ) (Fig. 9):

$$\begin{cases} F_{T\_chf} = \sum_{z=1}^3 [F_{c\_chf\ z} \times Y_{oi} + F_{n\_chf\ z} \times Y_{oi}] \\ F_{R\_chf} = -\sum_{z=1}^3 [F_{c\_chf\ z} \times X_{oi} + F_{n\_chf\ z} \times X_{oi}] \\ F_{A\_chf} = \sum_{z=1}^3 [F_{n\_chf\ z} \times Z] \end{cases} \quad (8)$$

$$\begin{cases} F_T = F_{T\_tip} + F_{T\_chf} \\ F_R = F_{R\_tip} + F_{R\_chf} \\ F_A = F_{A\_tip} + F_{A\_chf} \end{cases} \quad (9)$$

The precise angular position of the tool in the borehole during drilling ( $\theta_i$ ) can be easily calculated. But experimentally, this angular position is difficult to measure during a drilling test. Therefore, the simulation of the cutting forces along  $X$  and  $Y$  axis cannot be compared to experimental results as the shift angle cannot be identified. For this reason, the comparison between the modelling and the measurements was based on the resultant force applied on the tool in the plane perpendicular to its axis (noted  $F_{xy}$ ) and on the axial force  $F_z$ . From the measurements,  $F_{xy}$  can be calculated with the measured forces  $F_x$  and  $F_y$ :

$$F_{xy} = \sqrt{F_x^2 + F_y^2} \quad (10)$$

The measured forces  $F_{xy}$  and  $F_z$  can be respectively compared to simulated forces  $F_{RT}$  and  $F_A$ , where:

$$F_{RT} = \sqrt{F_R^2 + F_T^2} \quad (11)$$

The measured cutting forces are presented in Rey et al. [17]. The comparison between simulations and experimental measurements was performed considering the tool fully engaged into the material. Thus, in the paper, the entry and exit phases are not presented. Three tool revolutions are presented (Fig. 10).

It can be noted that the simulated axial force  $F_A$  represents with a good fidelity the axial forces generated in orbital drilling ( $F_z$ ).

The simulation of the resultant force  $F_{RT}$  shows also very good results. The characteristic evolution of this force is well simulated, in relation with the evolution of  $F_T$  and  $F_R$  explained above. So, the proposed model permits to represent and to explain the specific evolution of this bending force (in a plane perpendicular to the axis of the tool). Moreover, the amplitude of this effort is well predicted, which validates the modelling and the identification of the cutting parameters.

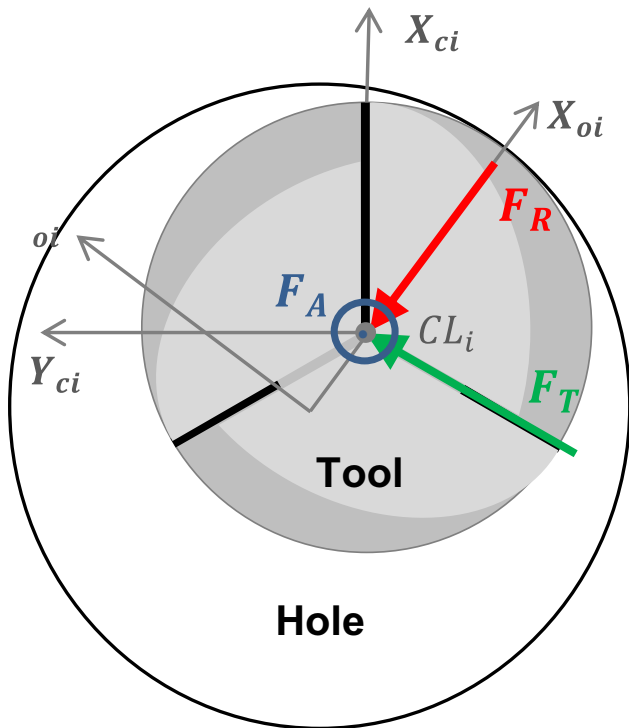
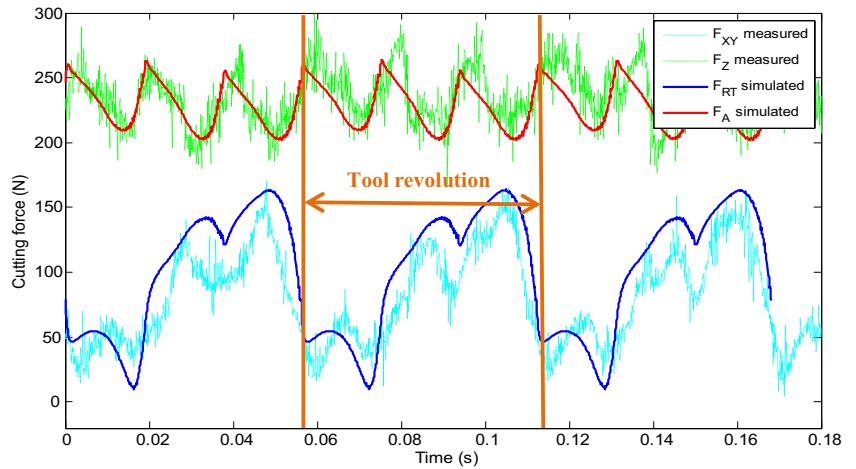


Fig. 9 Global cutting forces on the tool

Table 3 Summary of the identified coefficients [17]

	$K_c$	$q_c$	$K_c^* = K_c \times h^{-q_c}$ ( $h = 0.01$ mm)	$K_n$	$q_n$	$K_n^* = K_n \times h^{-q_n}$ ( $h = 0.01$ mm)	$K_{ind} \times s$	$q_{ind}$
Radial part	1643	0.229	4590	446	0.483	4124	-	-
Axial part	192.79	0.577	2750	48.505	0.811	2010	2.5887	1

**Fig. 10** Comparison of simulated and measured cutting forces.  $V_c = 30$  m/min;  $f_{za} = 0.005$  mm/tooth;  $f_{zt} = 0.04$  mm/tooth



As a result, the error between simulation and experimental results was assessed through the Bravais-Pearson correlation coefficients  $R_{RT}$  and  $R_A$ . For the transversal cutting force  $F_{RT}$ , the coefficient  $R_{RT}$  is 0.89. The mean error is 15 N, corresponding to 18.8%. This percentage is relatively high because of the low values of the cutting force. For the axial cutting force  $F_A$ , the coefficient  $R_A$  is 0.67. The mean error is 12 N, corresponding to 5.3%. These results reflect a high correlation between simulation and experimental results. The proposed modelling permits a good estimation of the forces generated in orbital drilling and can be used for the optimization of the process.

### 4 Influence of the tool geometry

#### 4.1 Influence of the geometry on the simulated cutting forces

Using the developed model, it is possible to simulate the cutting forces for different tool geometries and, thus, study the influence of this geometry. The goal is to correlate the tool tip geometry with the dimensional quality of the hole. This work will therefore focus on the forces having an impact on the final diameter and on the geometric quality of the hole.

The forces having an impact on the machined diameter are the forces that tend to bend the tool as a tooth is machining the surface of the hole. It was therefore chosen to study the force  $F_R$  when each tooth is in contact with the surface of the hole. Thus, the force ( $F_{RZi}$ ) is calculated when the tooth  $Z_i$  is in contact with the surface of the hole by considering the radial force  $F_R$  averaged over the area shown in Fig. 11. This zone is centered on the position where the tooth is in contact with the surface and represents  $5^\circ$  on each side of this position.

It is considered that the final surface of the hole is made by the tooth with the least effort because it is the tooth for

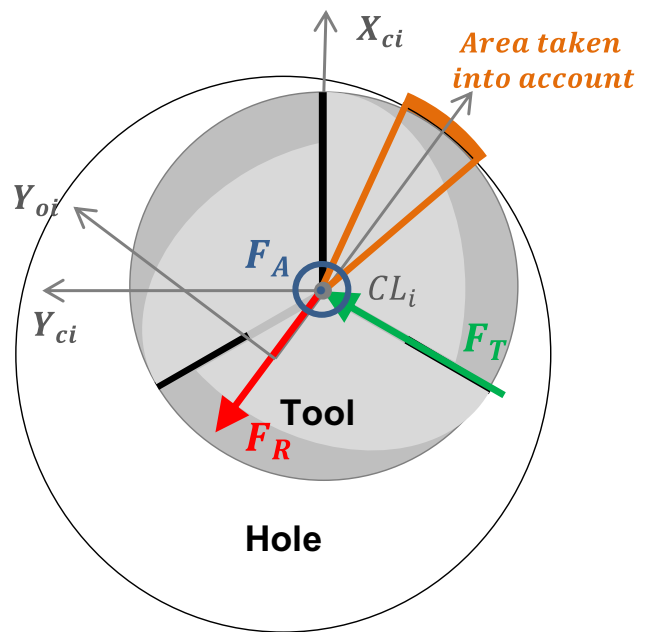


**Fig. 11** Area considered for the calculation of the effort  $F_R$

which the tool bending will be minimal. It is, therefore, this effort ( $F_{RZmin}$ ) that will be used to compare the different geometries.

Different tool tip geometries will be tested. For these simulations, the cutting conditions used are as follows:  $V_c = 30$  m/min ;  $f_{za} = 0.005$  mm/tooth;  $f_{zt} = 0.04$  mm/tooth.

As the geometry of the tool is complex, only a few characteristics will be studied. This work focuses on the axial zone of the tool. Indeed, it was identified that this zone is quite problematic. The tooth with the cut in the center was particularly fragile and wore very prematurely during the first holes. It is therefore interesting to study the utility of this center-cut and its impact on the drilling quality (Fig 12).

The cutting area close to the tool center is always an issue for axial tools because the cutting conditions at this location are greatly degraded by the very low or zero cutting speed. Regarding orbital drilling, it is easy to calculate the effective speed in the (X, Y) plane ( $V_{e\_XY}$ ) by considering the combination of the two rotations ( $N$  and  $N_{orb}$ ):

$$V_{e\_XY}(r_{Ai}, \varphi_i) = r_{Ai} \times 2\pi \times N - r_{ki}(r_{Ai}, \varphi_i) \times 2\pi \times N_{orb} \times \cos(\pi - \alpha(r_{Ai}, \varphi_i) - \varphi_i) \tag{12}$$

The evolution of the effective speed along the cutting edge (Fig. 13-a) shows that it tends towards a zero value close to the center of the tool as it is the case with axial drilling. However, by analyzing more precisely the area close to the center of the tool, the effective speed becomes even negative (Fig. 13b) due to the combination of the rotation of the tool and the orbital rotation. Thus, even if the orbital rotation seems negligible in comparison to the rotation speed of the tool, it can have a significant impact on the cutting conditions in the center of the tool. It explains why the axial zone is so problematic in orbital drilling.

Using the model, different tool geometries will be simulated to study the possibility of eliminating or reducing

the material to be cut in this area. The first task consisted in simulating material removal with a tool without a center-cut, so that all the teeth have a similar profile with a non-cutting radius at the center  $R_{cc}$  (Fig. 15).

This simulation shows that it is essential to keep a non-cutting radius at the center lower than the offset radius

( $R_{off}$ ) to ensure that the cutting tool can perform all of the machining. In this study, the non-cutting radius varied from 0 to 1.5 mm ( $R_{off}$ ) for a tool without a center-cut:  $R_{cc} = [0; 0, 5; 1; 1, 5]$ . For simulations with a tool having a center-cut, it is possible to have a non-cutting radius ( $R_{cc}$ ) greater than the interpolation radius ( $R_{off}$ ). In this case, the non-cutting radius varied from 0 to 2.5 mm:  $R_{cc} = [0; 0, 5; 1; 1, 5; 2; 2, 5]$ .

The other characteristics of the tool geometry remain identical to the tool used previously: three-flute tool ( $Z = 3$ ) of diameter  $D_t = 9$  mm, with a corner radius  $R_b = 1$  mm (Fig. 14).

The other parameter studied with the simulation was the tool cutting edge angle  $\kappa_r$ .

Fig. 12 Tooth wear with center-cut

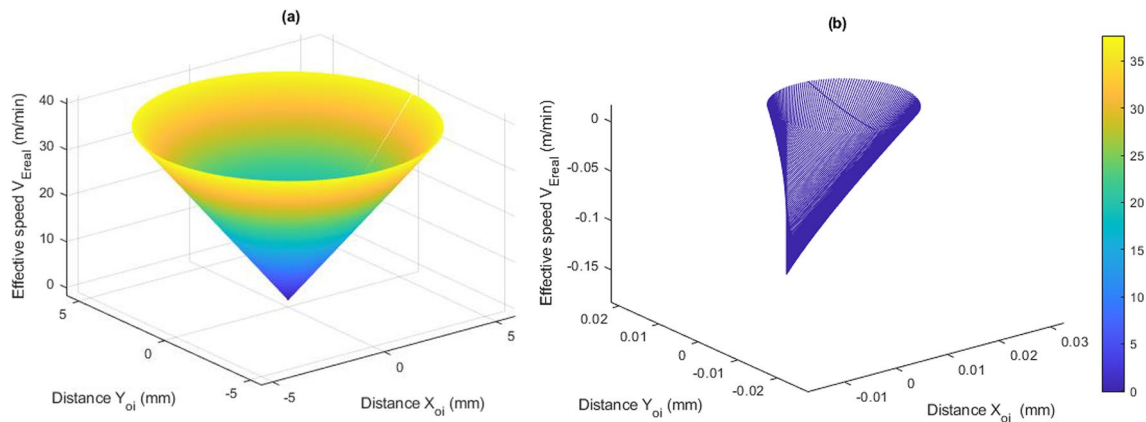
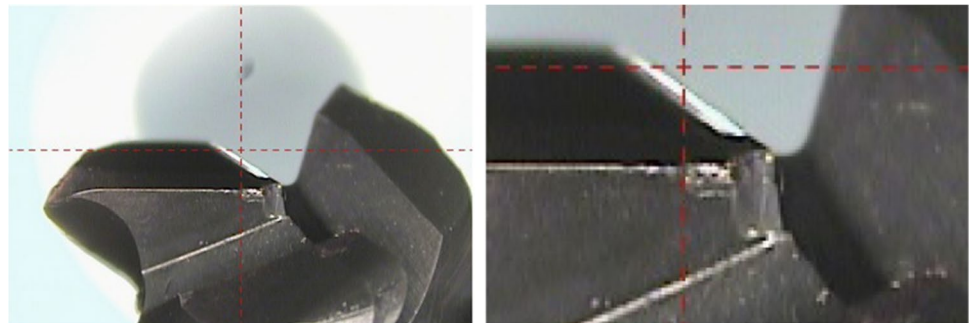


Fig. 13 Effective speed evolution during orbital drilling **a** entire tool **b** at the tool center ( $N = 1100$  tr/min;  $N_{orb} = 21$  tr/min)

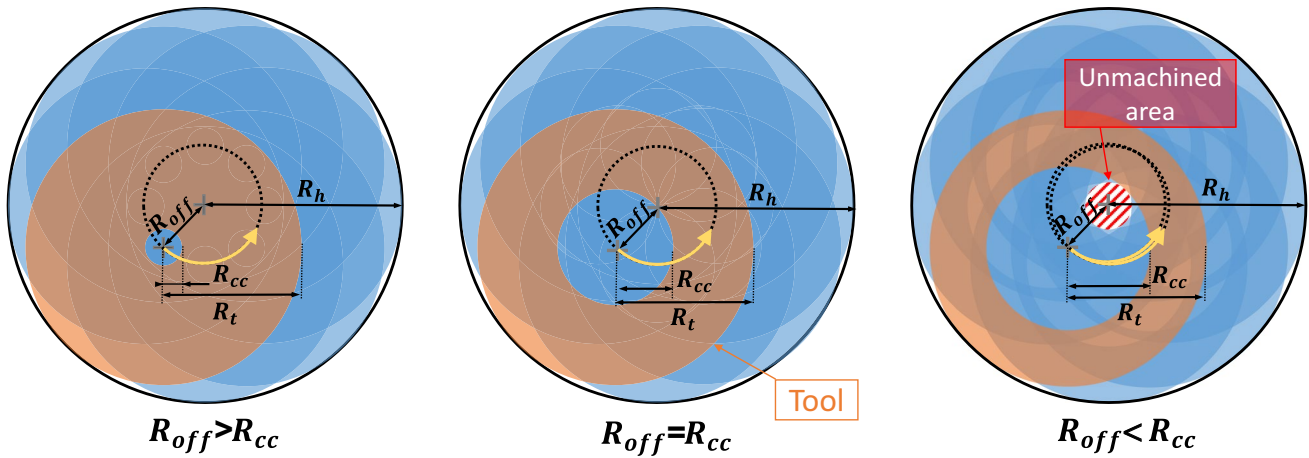


Fig. 14 Simulation of material removal for different values of the radius without center-cut

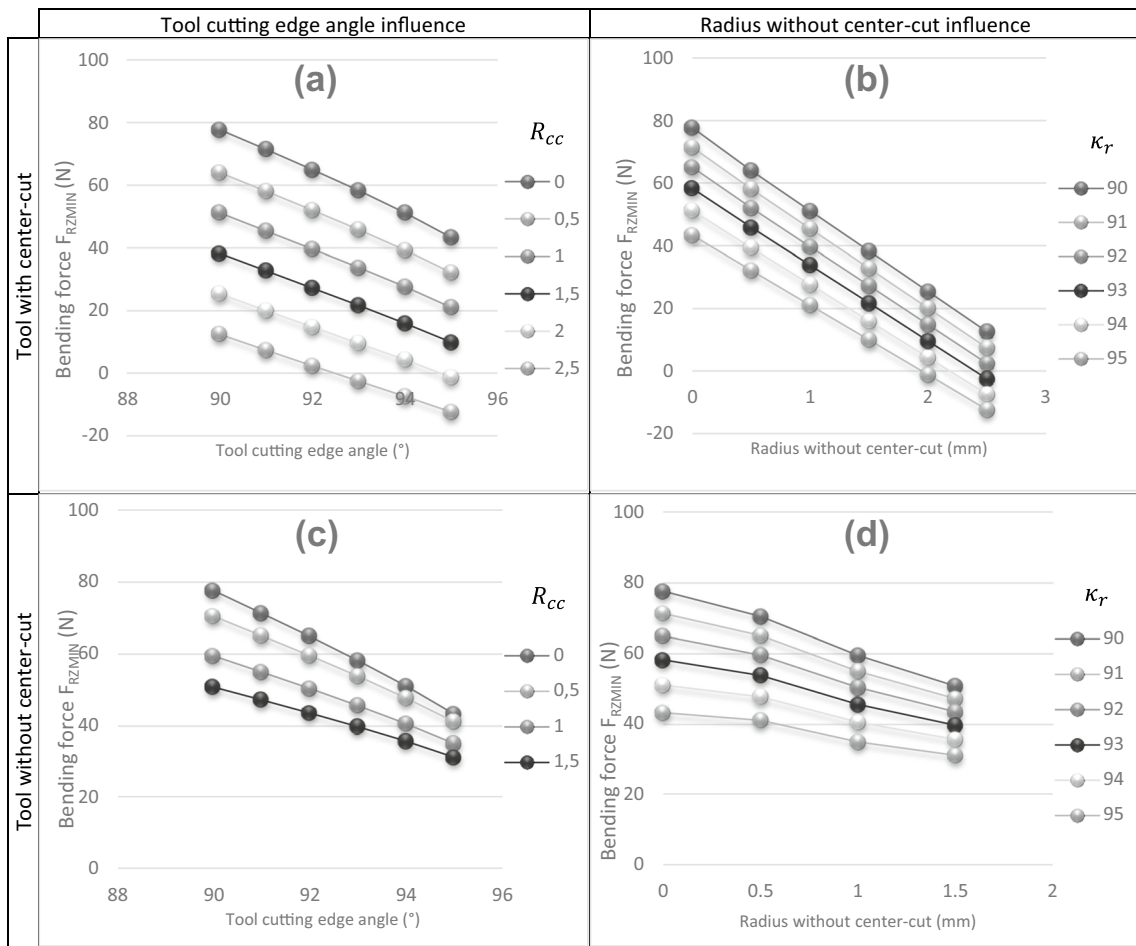


Fig. 15 Modelling results for the different geometries

The bending force ( $F_{RZmin}$ ) is simulated for the different tool geometries with the following cutting conditions:  $V_c = 30$  m/min;  $f_{za} = 0.005$  mm/tooth;  $f_{zt} = 0.04$  mm/tooth.

The result of all these simulations is presented in Fig. 15. These graphs show that in general, the increase of the tool cutting edge angle or of the radius without

center-cut leads to a decrease in the bending force  $F_{RZmin}$ . In the case of a tool with a center-cut, these variations are very significant, they go from 77 to -12N. This negative bending force means that the cutting forces generated by the three teeth tend to push the tooth machining the surface of the hole towards it. For the case of a tool without a center-cut, these variations are less important; the bending force goes from 77 to 31 N and never becomes negative.

To understand this result, the influence of these parameters on the evolution of the chip geometry of the axial part needs to be studied. The increase in radius without center-cut or the presence of a tooth with center-cut significantly modifies the geometry of the chip (Fig. 16). In Fig. 16a, the increase in the non-cutting radius causes an increase of the chip section at the back of the tool and a decrease of the chip section at the front of the tool. The presence of a center-cut has the same effect by increasing the chip section at the back of the tool (Fig. 16b). However, by working in down-milling, the forces generated by the machining of the back part of the tool are oriented so as to push the tool towards the surface of the hole and therefore counter the bending forces generated by the radial part of the tool. It is a reason why the minimal bending force decreases as the radius without center-cut increases (Fig. 15b-d).

Fig. 17 shows the influence of the tool cutting edge angle on the chip section. It can be noted that the chip

section at the back of the tool increases as the tool cutting edge angle increases.

This simulation explains the decreasing of the minimal bending force when the tool cutting edge angle increases (Fig. 16a-c).

In Fig. 10, the measured force  $F_{XY}$  and the modelled force  $F_{RT}$  show the successive passage of three teeth over the tool revolution. This is explained by the fact that the radial chip is not constant during the revolution of the tool. However, the differences between the peaks come from the presence of a single tooth with a center-cut. Thanks to the modelling, it is possible to study the evolution of the cutting forces to better understand the phenomena generated by the geometry of the axial part of the tool. The tool performance and the cutting phenomena caused by the radial part of the tool are known and considerably studied in the literature. The cutting phenomena on the axial part are more complex due to the combination of the geometry of the tool tip and the complex tool path.

To better understand the mechanisms during drilling, the evolution of the tangential force  $F_t$  at the contact point tool/work piece (according to Yoi) and of the radial force  $F_r$  (Fig. 18) was modelled only for the axial part.

During one revolution of the tool, these two forces oscillate strongly, which means that the bending force is highly variable. As a consequence, a dynamic phenomenon is established and must be studied to understand the chip thickness

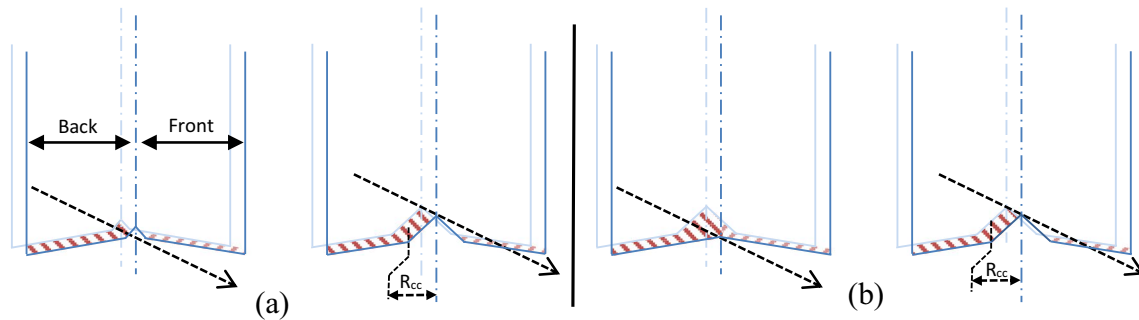
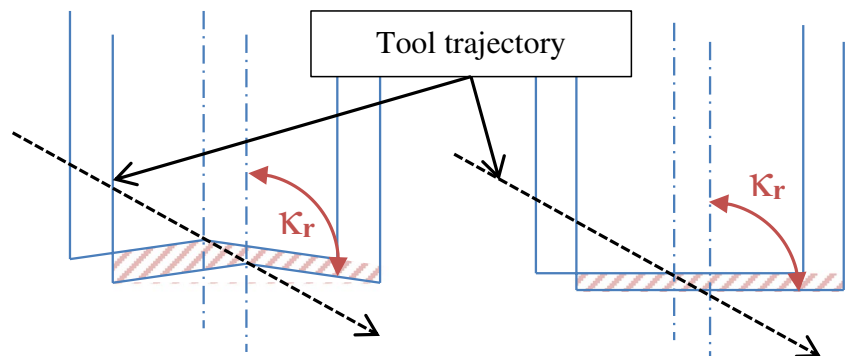
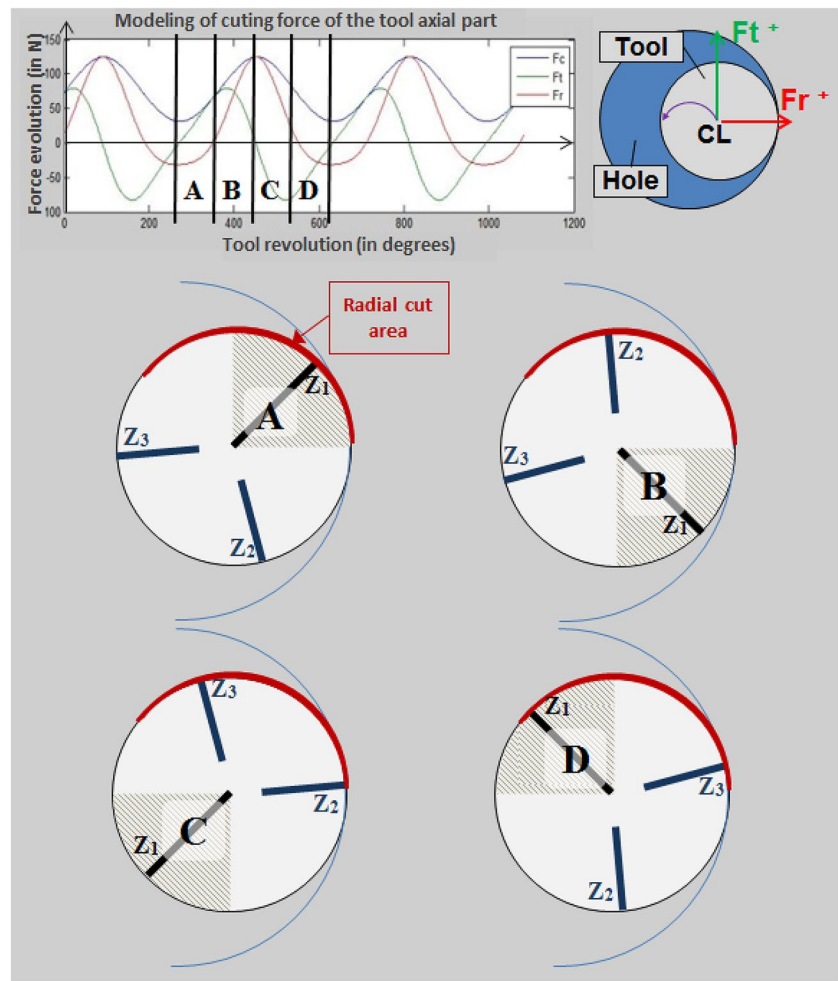


Fig. 16 Influence of the radius without center-cut (a) and the presence of the center-cut (b) on the geometry of the axial chip

Fig. 17 Influence of the tool cutting edge angle  $\kappa_r$  on the geometry of the axial chip



**Fig. 18** Modelling of the radial and tangential forces of the tool axial part, considering the three teeth



of the radial part. Fig. 18 shows that when the tooth with center-cut ( $Z_1$ ) is located in the “A” area ( $0 < \varphi < \frac{\pi}{2}$ ), the tangential force is positive, and the radial force is negative but quite low, not causing a significant modification in radial chip section. When the tooth with center-cut ( $Z_1$ ) is located in the “B” area ( $\frac{3\pi}{2} < \varphi < 2\pi$ ), the radial and tangential forces are both positive. Therefore, the resultant force tends to push the tooth being machined towards the surface. When the tooth with center-cut ( $Z_1$ ) is located in the area “C,” when the tooth ( $Z_2$ ) is in contact with the hole surface, the radial force is positive and the tangential force is negative. Therefore, the resultant force tends to push the tooth ( $Z_2$ ) towards the hole surface and in reverse tends to withdraw the tooth ( $Z_3$ ) from the hole surface. Finally, when the tooth with center-cut ( $Z_1$ ) is located in the area “D,” when the tooth ( $Z_3$ ) is in contact with the hole surface, the radial and tangential force are both negatives. Therefore, the resultant force tends to withdraw the tooth ( $Z_3$ ) from the hole surface.

The hypothesis is that the radial chip section is not homogeneous for the three teeth because bending forces are different for each passage of the various teeth on the radial cut

area. The radial chip thickness machined by the tooth ( $Z_2$ ) is greater than that machined by the tooth ( $Z_3$ ).

## 5 Results and discussions

To validate these simulations, orbital drilling tests were carried out. These tests were performed on a drill bench equipped with an orbital spindle. The cutting forces were recorded using the dynamometer Kistler and sampled at 10 kHz.

The hole diameter was 11.11 mm.

Three different tool geometries were tested (Fig. 19). Only the axial part was different. The first tool is the tool previously studied with a tool cutting edge angle ( $\kappa_r = 93^\circ$ ), one tooth with center-cut and the others with a radius without center-cut  $R_{cc} = 2\text{ mm}$ . The second tool is similar, only the tool cutting edge angle is different ( $\kappa_r = 90^\circ$  – flat tool tip). The third is similar to the second but without center-cut and with  $R_{cc} = 1.5\text{ mm}$ . All the tools used were especially made for the study.

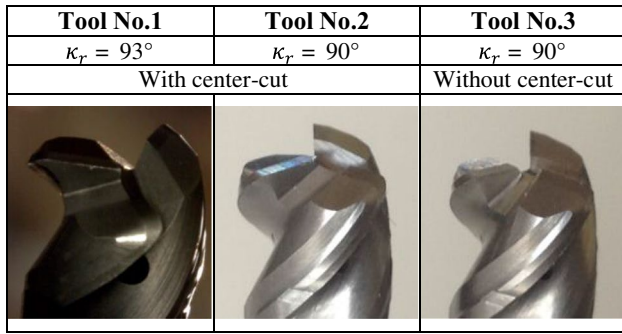
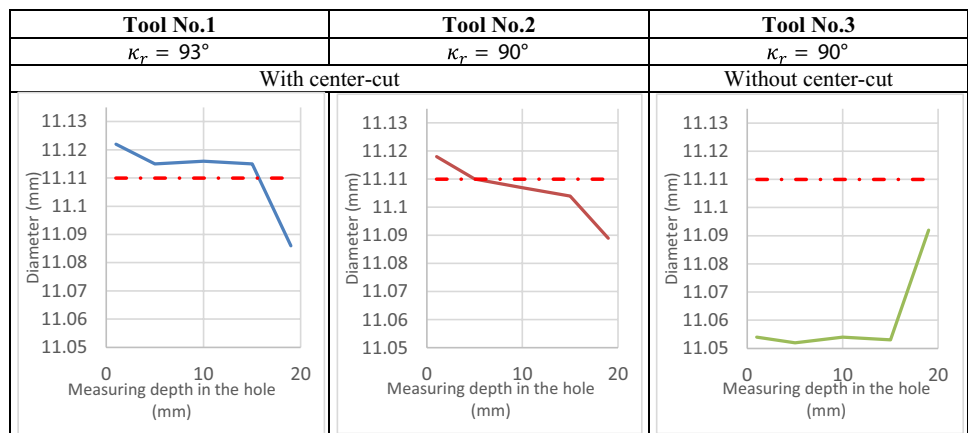


Fig. 19 The different tool geometries tested

The cutting conditions remained the same:  $V_c = 30$  m/min;  $f_{za} = 0.005$  mm/tooth;  $f_{zt} = 0.04$  mm/tooth.

A series of holes was performed with each tool, with the same conditions (material, cutting parameters, hole diameter). The diameter of the holes was measured on a three-dimensional coordinate measuring machine (CMM).

Fig. 20 Average profile measured on the hole for each tool



The results in terms of diameter (Fig. 20) show that the presence of a tooth with center-cut on the axial part of the tool has a significant impact on the hole profile due to the bending phenomena. The hole profiles obtained with the tools no. 1 and 2 show an entrance hole diameter larger than the output diameter. This validates the previous simulation results (Fig. 18): the axial part of the tool causes a positive average radial force, increasing the hole diameter. At the exit of the hole, the axial part is not anymore into the material; therefore, the diameter of the hole decreases due to tool bending caused by the radial part of the tool.

Between the first tool and the second, only the tool cutting edge angle is different. The influence of this angle on the axial chip is showed on Fig. 17. The chip section for the second tool is more homogeneous between the back and the front parts of the tool, which can be seen also on the modelled cutting forces (Fig. 21). The maximum radial force modelled for the second tool is around 70 N whereas it reaches 90 N for the first tool. It explains why the variation of hole diameter is less important for the second tool than for the first one.

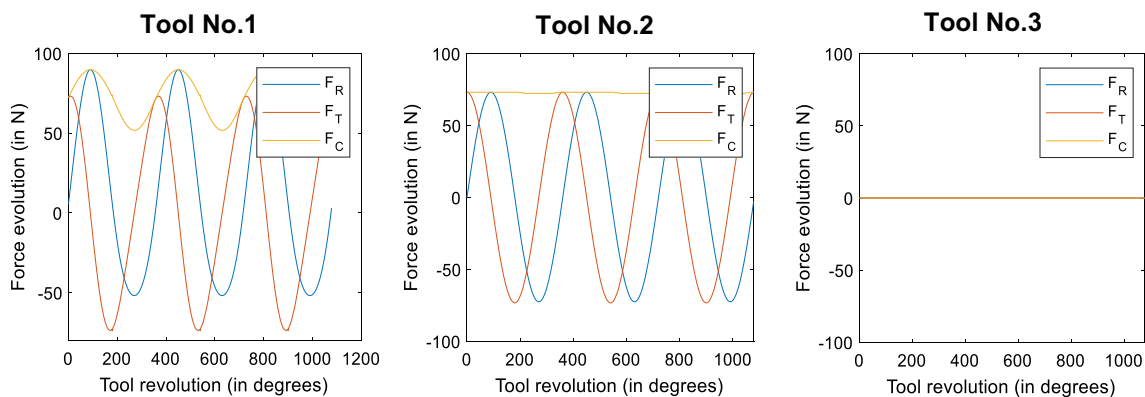


Fig. 21 Modelling of the cutting force of the tool axial part for the three tools

Considering the third tool, the three teeth are identical and the axial part is flat so the chip is identical for the three teeth. That is why the model shows no cutting force (Fig. 21), the forces on each tooth cancelling each other.

Without the radial force generated by the axial part, the tool is submitted to a bending force due to the radial part, generating a smaller diameter. The increase of diameter at the exit of the hole is due to the relaxation of the bending force as the tool exits the material progressively.

For tools no. 1, no. 2, and no. 3, the  $F_{RZmin}$  force is respectively 9.5 N, 25 N, and 50 N (Fig. 15), which reflects an increasing bending force for these tools and, therefore, a reduction in the drilled diameter. This agrees with the diameter measurements carried out (Fig. 20). The value of this force is difficult to use to accurately predict the final diameter because it would be important to take into account the dynamics of the cutting process. In addition, this force is extracted from a homogeneous cutting model over the whole of the axial part and comes from an estimate of a force at the center of the tool where the cutting conditions are strongly degraded for which the model has not been validated. However, this value appears to be an interesting criterion for optimizing the geometry of the tools and/or the cutting conditions in order to limit the tool bending.

## 6 Conclusions

In this paper, the use of a force model for orbital drilling permitted to study and to better understand the important role of the geometry of the axial part of the drilling tool. Models available in the literature were developed for simple flat-end tools. But industrial tools used in orbital drilling are more complex, and their geometry has a great influence on the process. In this paper, a model of chip geometry and cutting forces developed in previous work was used for simulating complex tool geometries. This model permits to simulate the complex chip geometry and the associated cutting forces and to dissociate the role of each part of the tool on the chip and forces generated, helping to better understand the cutting phenomena occurring in orbital drilling (e.g., tool bending). This model was thus used to study the impact of the geometrical characteristics of the tool. It allowed to better understand the forces generated during the orbital drilling process and made it possible to link the geometry of the tool to the geometry of the drilled hole.

This model can be used to optimize the cutting conditions and the tool geometry in relation to the cutting forces generated (in direction and in amplitude). Currently, the orbital drilling process struggles to meet the level of requirements of the aeronautical sector especially for the drilling of titanium alloys or multi-material stacks. The modelling

developed could permit to improve the performance of this process.

The development of an accurate prediction of the tool bending magnitude and of the dimensional quality of the hole will be conducted in future works. This will need to pursue the development of the model to consider the micro-geometry of the tool cutting edge and the evolution of wear, which remains a very critical point during the machining of this type of material.

**Code availability** The codes developed in this work are custom codes.

**Author contributions** All authors declare they have contributed to the study conception and design. Material preparation, data collection, and analysis were performed by P-AR. The first draft of the manuscript was written by P-AR, and all authors commented on previous versions of the manuscript. All authors read and approved the final manuscript.

**Funding** This work was carried out within the research project OPOSAP, funded by the region Midi-Pyrenees, the French state, and the European Commission. The work was also carried out within the context of the working group Manufacturing'21, which gathers 18 French research laboratories.

**Data availability** All data and materials are accessible.

## Declarations

**Ethics approval** The authors fully approve the journal's ethics policy.

**Competing interests** The authors declare no competing interests.

## References

1. Tönshoff H, Spintig W (1994) Machining of holes: developments in drilling technology. *Ann CIRP* 43:551–561
2. Lindqvist R, Eriksson I, Wolf M (2001) Orbital drilling of sandwich constructions for space applications. *SAE transactions* 179–186
3. Brinksmeier E, Fangmann S, Rentsch R (2011) Drilling of composites and resulting surface integrity. *CIRP Ann Manuf Technol* 60:57–60
4. Denkena B, Boehnke D, Dege J (2008) Helical milling of CFRP–titanium layer compounds. *CIRP J Manuf Sci Technol* 1(2):64–69
5. Ladonne M, Cherif M, Landon Y, K'Nevez J-Y, Cahuc O, De Castelabajac C (2015) Modelling the vibration assisted drilling process: identification of influential phenomena. *Int J Adv Manuf Technol* 81:1657–1666
6. Le Dref J, Landon Y, Dessein G, Espinosa C (2016) Modelling kinematics and cutting forces in vibration assisted drilling. *Mechanics & Industry* 17(3):301
7. Araujo AC, Landon Y, Lagarrigue P (2021) Smart drilling for Aerospace Industry: state of art in research and education. *Procedia CIRP* 99:387–391
8. Iyer R, Koshy P, Ng E (2007) Helical milling: an enabling technology for hard machining precision holes in AISI D2 tool steel. *Int J Mach Tools Manuf* 47:205–210
9. Brinksmeier E, Fangmann S (2009) Burr and cap formation by orbital drilling of aluminum. In: *Proceedings of the CIRP. International Conference on Burrs*, Kaiserslautern, Germany, pp 31–45

10. Sadek A, Meshreki M, Attia M (2012) Characterization and optimization of orbital drilling of woven carbon fiber reinforced epoxy laminates. *CIRP Ann Manuf Technol* 61:123–126
11. Ezugwu EO, Wang ZM (1997) Titanium alloys and their machinability a review. *J Mater Process Technol* 68(3):262–274
12. N. company, Orbital drilling inventor, 2018. [En ligne]. Available: <https://novator.eu>. Accessed 2018
13. Sun D, Lemoine P, Keys D, Doyle P, Malinov S, Zhao Q, Qin X, Jin Y (2018) Hole-making processes and their impacts on the microstructure and fatigue response of aircraft alloys. *Int J Adv Manuf Technol* 94:1719–1726
14. Pereira RBD, Brandão LC, de Paiva AP, Ferreira JR, Davim JP (2017) A review of helical milling process. *Int J Mach Tool Manu* 120:27–48
15. Ozturk OM, Kilic ZM, Altintas Y (2018) Mechanics and dynamics of orbital drilling operations. *Int J Mach Tool Manu* 129:37–47
16. Brinksmeier E, Fangmann S, Meyer I (2008) Orbital drilling kinematics. *Prod Eng* 2(3):277–283
17. Rey PA, LeDref J, Senatore J, Landon Y (2016) Modelling of cutting forces in orbital drilling of titanium alloy Ti-6Al-4V. *Int J Mach Tools Manuf* 106:75–88
18. Zhou L, Dong H, Ke Y, Chen G (2018) Modeling of non-linear cutting forces for dry orbital drilling process based on undeformed chip geometry. *Int J Adv Manuf Technol* 94:203–216
19. Zhou L, Dong H, Chen YKG (2017) Analysis of the chip-splitting performance of a dedicated cutting tool in dry orbital drilling process. *Int J Adv Manuf Technol* 90:1809–1823
20. Merchant ME (1945) Mechanics of the metal cutting process. *J Appl Phys* 16:267–275
21. Altintas Y, Kilic Z (2013) Generalized dynamic model of metal cutting operations. *Ann CIRP - Manuf Technol* 62(1):47–50
22. Denkena B, Köhler J (2010) Consideration of the form of the undeformed section of cut in the calculation of machining forces. *Mach Sci Technol* 14(4):455–470
23. Lorong P, Larue A, Perez Duarte A (2011) Dynamic study of thin wall part turning. *Adv Mater Res* 223:591–599
24. Kienzle O, Victor H (1957) Spezifische schnittkräfte bei der metallbearbeitung. *Werkstattstechnik und Maschinenbau* 47(5):224–225
25. Williams RA (1974) A Study of the Drilling Process. *ASME. J Eng Ind* 96(4):1207–1215. <https://doi.org/10.1115/1.3438497>
26. Stevenson R (1998) The measurement of parasitic forces in orthogonal cutting. *Int J Mach Tools Manuf* 38(1–2):113–130
27. Wyen CF, Wegener K (2010) Influence of cutting edge radius on cutting forces in machining titanium. *CIRP annals* 59(1):93–96

**Publisher's note** Springer Nature remains neutral with regard to jurisdictional claims in published maps and institutional affiliations.

Springer Nature or its licensor (e.g. a society or other partner) holds exclusive rights to this article under a publishing agreement with the author(s) or other rightsholder(s); author self-archiving of the accepted manuscript version of this article is solely governed by the terms of such publishing agreement and applicable law.